ORIGINAL PAPER

Grey area in embedded wall-modelled LES on a transonic nacelle-aircraft configuration

Marius Herr[1] · Axel Probst[2] · Rolf Radespiel[1]

Abstract

A scale-resolving hybrid RANS–LES technique is applied to an aircraft-nacelle configuration under transonic flow conditions using the unstructured, compressible TAU solver. In this regard, a wall-modelled LES methodology is locally applied to the nacelle lower surface to examine shock-induced separation. To circumvent the grey-area issue of delayed turbulence onset, a Synthetic Turbulence Generator (STG) is used at the RANS–LES interface. Prior to the actual examinations, fundamental features of the simulation technique are validated by simulations of decaying isotropic turbulence as well as flat plate flows. For the aircraft-nacelle configuration at a Reynolds number of 3.3 million, a sophisticated mesh with 420 million points was designed which refines 32 % of the outer casing surface of the nacelle. The results show a development of a well-resolved turbulent boundary layer with a broad spectrum of turbulent scales which demonstrates the applicability of the mesh and method for aircraft configurations. Furthermore, the necessity of a low-dissipation low-dispersion scheme is demonstrated. However, a noticeable drop of the surface skin friction downstream of the STG motivates further research on the impact of the interface modelling on the shock–boundary layer interaction.

Keywords Hybrid RANS–LES · Wall-modelled LES · Synthetic turbulence · Aircraft configuration · Transonic flow · Shock-induced separation

List of symbols

$\underline{\vec{A}}$	Cholesky decomposition of Reynolds stress tensor
AOR	Area of recirculation
α	Angle of attack
α_g	Geometrical function in WMLES blending function
α_e	Extrapolation parameter in central flux discretisation
c	Local chord length
c_f	Skin friction coefficient
c_p	Pressure coefficient
C_{DES}	Calibration constant in LES length scale
C_w	Constant in IDDES filter width
CFD	Computational fluid dynamics
CFL	Courant–Friedrichs–Lewy number
CTU	Convective time unit
$\vec{d}_{ij}$	Distance vector between points i and j
d_{refined}	Extension of refinement area in wall-normal direction
d_w	Wall distance
DIT	Decaying isotropic turbulence
DFG	German Research Foundation
DLR	German Aerospace Center
DNS	Direct numerical simulation
$\delta, (\delta_{STG})$	Boundary layer thickness (at position of STG)
$\delta_{\varphi,\min}(x)$	Minimum boundary layer thickness at position x
$\delta_{\varphi,\max}(x)$	Maximum boundary layer thickness at position x
Δ_0	Green–Gauss gradients
Δ_{IDDES}	Filter with of IDDES
$\Delta t, (\Delta t^+)$	(Non-dimensional) time step size

✉ Marius Herr
m.herr@tu-bs.de

Axel Probst
axel.probst@dlr.de

Rolf Radespiel
r.radespiel@tu-bs.de

1 Institute of Fluid Mechanics, TU Braunschweig, Hermann-Blenk-Str. 37, 38108 Braunschweig, Lower Saxony, Germany

2 Institute for Aerodynamics and Flow Technology, DLR, Bunsenstr. 10, 37073 Göttingen, Lower Saxony, Germany

Δx, (Δx^+)	(Non-dimensional) grid spacing in x-direction	Re_θ	Reynolds number with regard to momentum-thickness
$\Delta\varphi$, $(\Delta\varphi^+)$	(Non-dimensional) grid spacing in $\vec{e}_\varphi$-direction	ρ	Mass density
$\vec{e}_\varphi$	φ-base vector of cylindrical coordinate system	s	Mode frequency
ETW	European Transonic Windtunnel	SST	Menter's Shear-Stress Transport turbulence model
(E)WMLES	(Embedded) wall-modelled Large Eddy Simulation	STG	Synthetic Turbulence Generator
f_B	WMLES blending function	$\vec{\sigma}$	Directional vector
$\tilde{\tilde{f}}_d$	Main blending switch of IDDES	σ_b	Blending function in hybrid LD2 scheme
f_{dt}	IDDES delaying function	t, t'	Time
f_e	IDDES elevating function	TAU	Compr. flow solver provided by German Aerospace Center
FOR 2895	Research Unit of the German Research Foundation	TKE	Turbulent kinetic energy
HGF	Helmholtz Association	τ	Time scale
(H)LD2	(Hybrid) low-dissipation low-dispersion numerical scheme	UHBR	Ultra High Bypass Ratio
		(U)RANS	(Unsteady) Reynolds-averaged Navier-Stokes equation
$h_{\max}$	Maximum local edge length	$\vec{u}$	Velocity vector
h_{wn}	Grid spacing in wall-normal direction	$\vec{u'}$	Velocity fluctuation vector
(ID)DES	(Improved Delayed) Detached Eddy Simulation	$\langle\vec{u}\rangle$	Temporal average of velocity vector
k, (k^+)	(Normalised) wave number	$\vec{u}'_{ST}$	Injected velocity fluctuations by STG
$\kappa^{(4)}$	Global scaling factor in LD2 scheme	$u_{\inf}$	Magnitude of farfield velocity
l_{hyb}	Hybrid length scale	x	X-coordinate
l_{LES}	LES length scale	XRF1	Airbus research configuration
l_{RANS}	RANS length scale	x_i	Location of flow characteristic i in x-direction
LES	Large Eddy Simulation	y	Y-coordinate
Ma	Mach number	Δy^+	Non-dimensional grid spacing in y-direction
mean-c_f	Temporally averaged c_f		
mean-c_p	Temporally averaged c_p	z	Z-coordinate
μ_l	Laminar dynamic viscosity	ZIB	Zuse Institute Berlin
μ_t	Turbulent dynamic viscosity	ζ	Coordinate direction
N	Number of Fourier modes		
n	Time step		
NHR	Nationales Hochleistungsrechnen		
Ω_i	Subregion i of refinement region		
PSP	Pressure-sensitive paint		
Φ	Skew-symmetric central flux		
ϕ	Mode phase		
φ	Angular coordinate of cylindrical coordinate system		
Ψ_i	Parameter set i		
$\vec{Q}$	Partial time derivative of synthetic fluctuations		
q	Normalised mode amplitudes		
r	Radial coordinate of cylindrical coordinate system		
$\vec{r}'$	Position vector		
Re	Reynolds number		
Re_∞	Farfield Reynolds number		
Re_δ	Reynolds number with regard to boundary layer thickness		

1 Introduction

Transonic flows about aircraft configurations exhibit complex, unsteady flow phenomena such as oscillating shock fronts with boundary layer separation. This so-called buffet phenomenon causes unsteady aerodynamic loads which might endanger the flight safety. Therefore, a fundamental understanding of the related flow physics is of particular interest to be able to find specific technical solutions which control this phenomenon. The present study examines a XRF1 aircraft model which represents a wide-body long-range configuration and was designed by Airbus. An Ultra High Bypass Ratio (UHBR) nacelle is coupled to the model which represents a modern and efficient jet engine that is modelled as flow-through nacelle for wind tunnel testing. Due to the large circumference of the nacelle, a close coupling by means of a pylon to the wing lower side is necessary. This channel-like arrangement of nacelle, pylon, wing and fuselage causes the development of an

accelerated flow which triggers the formation of transonic shocks within this area. Depending on the exact flow conditions, these shocks evolve into buffet with significant loads. Initial investigations in the framework of the DFG (Deutsche Forschungsgemeinschaft) funded research group have shown a complex system of shock fronts [1]. As a first step toward representing this complex system with a sophisticated numerical method, this study focuses on a single shock front located at the lower side of the nacelle.

Numerous numerical investigations have investigated the problem of buffet onset with well-established unsteady Reynolds-averaged Navier–Stokes (URANS) methods. However, it is well known that even highly developed Reynolds stress-based URANS models show deficiencies in describing the dynamics of separated boundary layer as well as the aerodynamic effects of large flow separations [2]. Also, due to high, flight relevant Reynolds numbers a broad scale of turbulent structures arise for the given flow phenomenon. Therefore, a simulation technique that provide both high spatial and temporal resolution is required.

Direct Numerical Simulation (DNS) resolves all turbulent scales but is so far restricted to simple geometries at low Reynolds numbers due to its unfeasible computational effort for flight relevant flows. For this reason, a Large Eddy Simulation (LES) technique is required which only resolves large turbulent scales, whereas small, isotropic scales are modelled. Since an application of LES to the entire aircraft configuration is still computationally too expensive, a hybrid RANS–LES technique is employed. In the present study, the wall-modelled LES (WMLES) method within the Improved Delayed Detached Eddy simulation (IDDES) methodology is used [3]. Depending on the spatial discretisation, up to 5 % of the wall adjacent boundary layer is modelled by the RANS equations. Additionally, the area of WMLES is embedded around the transonic shock such that all relevant flow areas are enclosed. This corresponds to 32 % of the outer casing surface of the nacelle. The remaining flow field of wing, body, pylon and nacelle is modelled with an URANS model. The embedded WMLES (EWMLES) requires an injection of synthetic turbulence at the RANS–LES interface which is located at the leading edge of the nacelle for the present configuration. Otherwise, a so-called grey area would arise which describes a region of underresolved turbulence directly downstream of the RANS–LES boundary. To this end, the Synthetic Turbulence Generator (STG) devised by [4] is employed. Nevertheless, using this method, a transitional region from modelled to fully resolved turbulence is still present and is referred to as adaption region in this study. The analysis of this adaption region with regard to its length and behaviour of relevant flow quantities in this area are of major interest. Thus, especially the transient establishment of resolved turbulence within the WMLES area and

the fundamental applicability of the method to the aircraft configuration are the focus of this study.

The study is structured as follows. The employed WMLES model in conjunction with the STG is described in detail in Sect. 3.1 and 3.2, respectively. Subsequently, a thorough description of the employed low-dissipation low-dispersion (LD2) numerical scheme is given in 3.3. Section 4 provides a basic validation of the Embedded WMLES based on the SST-RANS model by means of flows of decaying isotropic turbulence and a flow about a flat plate. The results of the application to the XRF1 configuration are presented in Sect. 5. An extensive description of the mesh design with regard to the extension of the WMLES area, the used refinement criteria and its application to the actual mesh environment are presented (Sect. 5.2). Results of the transient WMLES establishment are then shown and assessed in Sect. 5.3. The analysis of temporally and spatially averaged flow quantities in the area related to the STG is carried out (Sect. 5.4). Finally, sensitivity studies with regard to the position of the RANS–LES boundary (Sect. 5.5.1) and the effect of using a standard numerical scheme instead of the low-dissipation scheme (Sect. 5.5.2) is presented. This paper is closed by a final summary of all research findings (Sect. 6).

2 Numerical methods

The flow simulations in this paper use the unstructured compressible DLR-TAU code [5] which numerically solves the flow and model equations on mixed-element grids (e.g. hexahedra, tetrahedra, prims) via the finite-volume approach. It applies 2nd-order discretization schemes for both space and time, together with low-Mach-number preconditioning for flows that are close to the incompressible limit. Implicit dual-time stepping allows adapting the time step in unsteady simulation to the physical requirements (i.e. related to the convective CFL criterion), avoiding numerical stability restrictions.

The relevant methods for embedded wall-modelled LES, i.e. the overall (hybrid) turbulence model, the method to generate and inject synthetic turbulence and the required local adaptation of the numerical scheme, are outlined in the following.

2.1 Hybrid RANS–LES Model

The present embedded wall-modelled LES approach relies on the Improved Delayed Detached Eddy Simulation (IDDES) [3] which combines local RANS, DES (i.e. RANS–LES) and wall-modelled LES (WMLES) functionalities in a seamless, automatic manner. This is achieved by a single *hybrid* length scale replacing the integral

turbulent scale l_{RANS} in the underlying RANS model, which is the two-equation SST model [6] in the present work. The hybrid length scale reads

$$l_{\mathrm{hyb}} = \tilde{f}_d \left(1 + f_e\right) l_{\mathrm{RANS}} + \left(1 - \tilde{f}_d\right) l_{\mathrm{LES}}. \tag{1}$$

Here, the function $\tilde{f}_d = \max\left\{(1 - f_{dt}), f_B\right\}$ is the main blending switch between the different modelling modes, where f_{dt} and f_B depend on local grid and flow properties (cf. [3]). f_B is defined as follows:

$$f_B = \min\{2\exp(-9\alpha_g^2), 1.0\}, \tag{2}$$

$$\alpha_g = 0.25 - d_w / h_{\max}, \quad h_{\max} = \max\{\Delta x, \Delta y, \Delta z\}, \tag{3}$$

where d_w and $\Delta\zeta$ are defined as the wall distance and the local cell length in the coordinate direction ζ, respectively. The additional *elevating* function f_e is designed to avoid a damping of the modelled Reynolds stresses in the intersection region between the RANS and LES modes, thus reducing the well-known log-layer mismatch in WMLES. However, it was demonstrated with the aid of various attached and separated flows that the impact of f_e is of minor importance for SST-IDDES [7]. We therefore assume that the influence of f_e is also of minor relevance for the present flow.

In WMLES mode ($f_{dt} \equiv 1$ and, thus, $\tilde{f}_d \equiv f_B$), if resolved turbulent content enters an attached boundary layer, a RANS layer is kept near the wall and sized according to the local grid resolution, thus circumventing the extreme grid requirements of wall-resolved LES at high Reynolds numbers. However, since no wall functions are applied in the present work, the equations need to be solved down to the wall with a (normalised) near-wall grid spacing of $\Delta z^+ \leq 1$.

In the largest (outer) parts of the boundary layer, $l_{hyb} \equiv l_{\mathrm{LES}} = C_{\mathrm{DES}}\Delta$, which approximates the behaviour of a Smagorinsky-type sub-grid model for LES. The model constant C_{DES} is usually calibrated for canonical turbulent flow, such as decaying isotropic turbulence (DIT); see Sect. 4.1. However, since wall-bounded flows typically require a different calibration than free turbulence, another modification compared to standard DES/LES is introduced in the filter width Δ:

$$\Delta = \Delta_{\mathrm{IDDES}} = \min\left\{\max\left[C_w \cdot d_w, C_w \cdot h_{\max}, h_{wn}\right], h_{\max}\right\} \tag{4}$$

where $C_w = 0.15$ and h_{wn} represents the grid spacing in wall normal direction.

In essence, this near-wall limitation of the filter width compensates for this flow-type dependency and allows using an unique C_{DES} value for both wall-bounded and off-wall turbulent flow. More details on this modification are found in [3].

For embedded WMLES, the IDDES in TAU can be locally forced to WMLES mode according to external user input, e.g. inside boxes or other suitable geometric sub-areas of the flow domain. This is achieved by setting the function f_{dt} to 1 downstream of the desired RANS-WMLES interface, thus safely reducing the eddy viscosity from RANS to WMLES level [8]. An additional damping of modelled turbulence at the RANS–LES interface is not employed and also not required as demonstrated in Sect. 5.4.

2.2 Synthetic turbulence generation

In this work, synthetic turbulent fluctuations at the streamwise RANS–LES interface are provided by the Synthetic Turbulence Generator (STG) of Adamian and Travin [9] with extensions for volumetric forcing by Francois [10]. This STG generates local velocity fluctuations from a superimposed set of N Fourier modes as

$$\vec{u}'_{ST} = \underline{\vec{A}} \cdot \sqrt{6} \sum_{j=1}^{N} \sqrt{q^j} \left[\vec{\sigma}^j \cos\left(k^j \vec{d}^j \cdot \vec{r}' + \phi^j + s^j \frac{t'}{\tau}\right)\right] \tag{5}$$

where the direction vectors $\vec{d}^j$ and $\vec{\sigma}^j \perp \vec{d}^j$, the mode phase ϕ^j, and the mode frequency s^j are randomly distributed. A realistic spectral energy distribution of the mode amplitudes q^j is achieved by constructing a von Kármán model spectrum from RANS input data and a local grid cut-off. The RANS data, which are automatically extracted from just upstream the RANS–LES interface, are also used to scale the fluctuations via the Cholesky-decomposed RANS Reynolds stress tensor $\underline{\vec{A}}$.

For realistic temporal correlations in a volumetric forcing domain, the position vector $\vec{r}'$ and the time t' are modified in accordance with Taylor's frozen velocity hypothesis, see [10] for details.

Synthetic turbulence injection To inject the synthetic fluctuations from Eq. (5), a forcing volume with a streamwise extent of about half the local boundary layer thickness is marked just downstream of the RANS–LES interface. Inside this volume, a momentum source term is added [11] which approximates the partial time derivative of the synthetic fluctuations as

$$\vec{Q} = \frac{\partial\left(\rho\vec{u}'_{ST}\right)}{\partial t} \approx \frac{3\left(\rho\vec{u}'_{ST} - \rho\vec{u}'^n\right) - \left(\rho\vec{u}'^n - \rho\vec{u}'^{n-1}\right)}{2\Delta t}. \tag{6}$$

This discretization corresponds to the 2nd-order backward difference scheme used for unsteady simulations with TAU. By computing the fluctuation values of the previous time steps from the actual flow field, i.e. as $\vec{u}'^n = \vec{u}^n - \langle\vec{u}\rangle$ and $\vec{u}'^{n-1} = \vec{u}^{n-1} - \langle\vec{u}\rangle$, the synthetic target field (Eq. 5) can be reproduced rather accurately in the simulation, even though

running time averages are required. An additional Gauss-like blending function with a maximum value of 1 around the streamwise centre of the forcing volume is multiplied to the source term to prevent abrupt variation of the forcing.

2.3 Hybrid low-dissipation low-dispersion scheme

Since scale-resolving simulation methods like IDDES involve explicit modelling of the sub-grid stresses, the overall accuracy relies on low spatial discretisation errors in the LES regions of a given grid. Concerning resolved turbulence, there are two types of error that mainly stem from the discretised convection of momentum: while numerical dissipation damps the turbulent fluctuations and would lead to under-predicted Reynolds stress, numerical dispersion distorts the shape of resolved turbulent structures.

For that reason, the present simulations apply a hybrid low-dissipation low-dispersion scheme (HLD2) [12], which combines different techniques to optimise the convection scheme for local scale-resolving simulations using unstructured finite-volume solvers.

To provide low numerical dissipation, the spatial fluxes are calculated from Kok's [13] skew-symmetric central convection operator, which allows for kinetic energy conservation (i.e. it is non-dissipative) on curvilinear grids in the incompressible limit. For compressible flow on general unstructured grids, a classic blend of 2nd-/4th-order artificial matrix-dissipation is added to ensure stability around shocks and in smooth flow regions. Compared to RANS computations, however, the 4th-order dissipation has been strongly reduced by manually optimising its parameters in LES computations of the channel flow, yielding, e.g. a global scaling factor of $\kappa^{(4)} = 1/1024$ and a reduced Mach-number cutoff in the low-Mach-number preconditioning matrix.

Moreover, to minimise the dispersion error of the second-order scheme, the skew-symmetric central fluxes are based on linearly reconstructed face values $\phi_{L,ij}, \phi_{R,ij}$ using the local Green–Gauss gradients $\nabla_0 \phi$. A generic central flux term reads

$$\phi_{ij,\alpha_e} = \frac{1}{2}\left(\phi_{L,ij} + \phi_{R,ij}\right) = \frac{1}{2}\left(\phi_i + \phi_j\right) + \frac{1}{2}\alpha_e\left(\nabla_0\phi_i - \nabla_0\phi_j\right)\cdot\vec{d}_{ij}, \tag{7}$$

where $\vec{d}_{ij}$ is the distance between the points i and j. With an extrapolation parameter of $\alpha_e = 0.36$, the scheme was found to minimise the required points per wavelength for achieving a given error level in a 1D wave problem; see [14] for details.

2.4 Blended scheme for hybrid RANS–LES

While the low-error properties of the LD2 scheme are essential for accurate LES and WMLES predictions with TAU [12], the pure RANS and outer flow regions in hybrid RANS–LES are less dependent on such numerical accuracy.

Moreover, although the LD2 scheme has been globally applied in hybrid RANS–LES, complex geometries like the present XRF1 configuration and corresponding unstructured grids may induce local numerical instabilities that are not damped by low-dissipative schemes. For this reason, we apply the LD2 scheme in a hybrid form [12] where all parameters of the spatial scheme, Ψ_i, are locally computed from a blending formula:

$$\Psi_i = (1 - \sigma_b) \cdot \Psi_{i,\text{LD2}} + \sigma_b \cdot \Psi_{i,\text{Ref}}. \tag{8}$$

Here, $\Psi_{i,\text{LD2}}$ are the parameter values of the LD2 scheme (e.g. $\kappa^{(4)} = 1/1024$, $\alpha_e = 0.36$), whereas $\Psi_{i,\text{Ref}}$ corresponds to standard central scheme parameters typically used in RANS computations (e.g. $\kappa^{(4)} = 1/64$, $\alpha_e = 0$). The blending function σ_b is adopted from [4] and discerns between the well-resolved vortex-dominated flow regions (*LD2*) and coarse-grid irrotational regions (reference scheme).

By now, the hybrid LD2 scheme (HLD2) has been successfully applied in a number of hybrid RANS–LES computations ranging from canonical flows on structured grids [12] to complex high-lift aircraft on mixed-element unstructured meshes [15].

3 Basic validation of embedded WMLES

Before analysing the embedded WMLES approach from Sect. 3 for a complex transonic aircraft configuration with UHBR nacelle in Sect. 5, we investigate and demonstrate its basic scale-resolving functionalities in fundamental test cases, i.e. decaying isotropic turbulence for pure LES and a developing flat-plate boundary layer for WMLES.

3.1 Decaying isotropic turbulence

Although SST-based IDDES is a well-known hybrid model present in many CFD codes, a proper verification for a given flow solver and the applied numerical scheme requires fundamental tests of the different modelling modes. This includes the pure LES functionality, where the hybrid model acts as Smagorinsky-type sub-grid model and mostly relies on the "outer-flow" calibration constant of SST-based IDDES, i.e. $C_{\text{DES}} = 0.61$.[1]

For this reason, we present for the first time TAU simulations of decaying isotropic turbulence (DIT) using SST-IDDES with the LD2 scheme and compare the results with classic experimental data from [16]. In particular,

---

[1] Note that the calibration constant in SST-based DES-variants takes a different value close to walls, but this region is usually treated in RANS mode anyway.

Fig. 1 TKE spectra of decaying isotropic turbulence (DIT) for two different times along with experimental data [16]. Results for the LD2 scheme (left) and a reference central scheme (right) are shown, with $C_{DES} = 0.61$
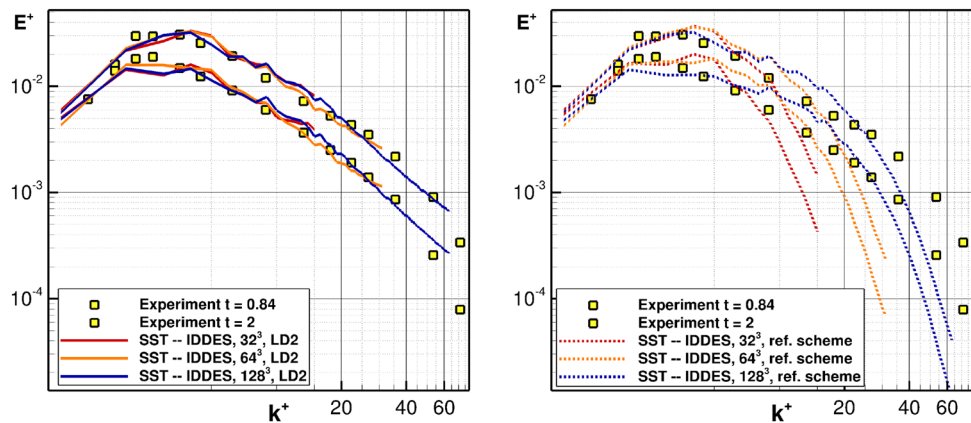
the turbulent-kinetic-energy (TKE) spectra at two different time levels after the start of decay, i.e. $t = 0.87$ s and $t = 2.0$ s, are considered. Additionally, to emphasise the effect of the LD2 scheme, further SST-IDDES simulations are performed using a reference central scheme with higher artificial dissipation (cf. Eq. 8 in Sect. 3.3). Note that we retain the original calibration of C_{DES} in SST-IDDES [3] during this study and throughout the paper.

As for the computational setup, a cubic domain with normalised edge length of 2π is discretised by Cartesian meshes with 32^3, 64^3 and 128^3 cells, respectively. Periodic boundary conditions are applied in all three directions. The initial velocity field has been generated by a Kraichnan-type synthetic turbulence approach [17] and retains the TKE spectrum of the experiment at $t = 0$ s. Due to the compressible formulation of the DLR-TAU code, appropriate initial density and pressure fields are derived from the isentropic relations of compressible fluids, describing the change of state from stagnation ($Ma_\infty = 0$) to the local Mach number, i.e. $\rho/\rho_\infty = f(Ma)$ and $p/p_\infty = f(Ma)$. Moreover, the initial fields of modelled TKE and specific dissipation rate ω are computed in a preliminary steady-state SST-IDDES computation, where all equations except for the hybrid turbulence model are frozen. The temporal resolutions of $\Delta t/s \in \{5 \cdot 10^{-3}, 5 \cdot 10^{-3}, 2 \cdot 10^{-3}\}$ for the coarse, middle and fine grid were determined in time step convergence studies.

Figure 1 (left) shows the results for the SST-IDDES with LD2 scheme which demonstrate a good agreement with the experimental results for all spatial resolutions and both time levels. For the reference central scheme, however, the picture is different. Although there are agreements with the experimental results for small wave numbers scales $k^+ \leq 8$ for all resolutions and time levels, deviations arise for larger wave numbers. These deviations are growing with increasing wave number and finally result in a significant underestimation of the TKE for all setups.

As a result, we successfully demonstrated the LES functionality of SST-IDDES in conjunction with the LD2 scheme. The low-dissipation feature of the numerical scheme was confirmed and additionally emphasised by reference simulations with higher artificial dissipation.

3.2 Developing flat-plate boundary layer

For a basic assessment of the full-embedded WMLES functionality, we consider the test case of a developing flat-plate boundary layer, which transitions from RANS to WMLES at a fixed streamwise position. It starts with zero thickness at the inflow and is computed in SST-RANS mode up to the position, where the momentum-thickness Reynolds number reaches $Re_\theta = 3040$. Here, a zonal switch to WMLES within IDDES is placed, along with a synthetic turbulence forcing region of about half a boundary layer thickness in the streamwise direction; see Sect. 3.2.

A hybrid grid with 5.8 million points and hexahedral cells in the WMLES area is used, which ensures $\Delta x^+ \approx 100 - 200$ in streamwise direction, $\Delta y^+ \approx 50$ in spanwise direction and $\Delta z^+ \approx 0.2$ in wall-normal direction similar to the structured grid used in [18]. The heights of the near-wall cells Δz^+ are limited to 0.2 to safely fulfil the resolution requirements of the RANS-SST model, which is $\Delta z^+ \leq 0.4$ for the employed numerical setup in the DLR-TAU code. More relevant for WMLES, the streamwise spacing fulfils $\Delta x \leq \delta/10$ throughout the flow domain, where δ is the approximate local boundary layer thickness. The normalised time step (in wall units) is $\Delta t^+ \approx 0.4$ and safely fulfils the convective CFL criterion (CFL$_{conv} < 1$) in the whole LES region. The statistical input data for the STG methods are given by external input from a precursor RANS profile at $Re_\theta = 3040$ which has been augmented with an anisotropic normal-stress approximation according to [19].

The spanwise and temporal averaged results of the skin friction distribution mean-c_f are depicted in Fig. 2 (red

Fig. 2 Evolution of averaged skin friction along streamwise position x of the flat plate test case for different wall-normal resolutions Δz^+
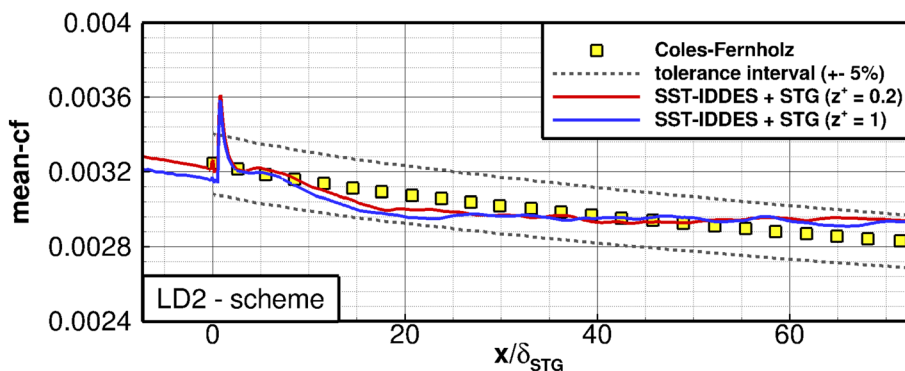
curve) along with the Coles–Fernholz correlation [20]. After an initial overshoot of mean-c_f at the position of the STG, mean-c_f shows acceptable agreements with the Coles–Fernholz correlation and remains within an acceptable error margin of 5 %. Note that an adaption region downstream of the STG is not visible in the presented results. The adaption region is defined as underestimation of mean-c_f compared to the previous mean-c_f level directly upstream of the STG. A further discussion of possible factors influencing the c_f-adaption region is given in Sect. 5.6.

For further sensitivity analyses, the influence of the wall-normal grid resolution was studied. To this end, an additional mesh, where z^+ was increased to $z^+ = 1$, was constructed. Since the growth rate of the cell heights in wall-normal direction remained unchanged, this coarsening affects the whole boundary layer grid. Relevant differences between the two flow solutions occur in the RANS region directly upstream of the STG. For the coarsened mesh, the skin friction falls below the reference values of the Coles–Fernholz correlation. This confirms that the SST-RANS computations require a comparatively high wall-normal resolution ($\Delta z^+ \leq 0.4$). In the WMLES area, however, ($x/\delta_{STG} \geq 0$), the underestimation of the c_f distribution decreases compared to the red curve ($\Delta z^+ = 1$) and even disappears for ($x/\delta_{STG} \geq 25$) so that both curves are rather close to each other. As a result, the impact of the wall-normal resolution is limited to the upstream RANS region, while the WMLES region is hardly affected. Nevertheless, the authors adhere to the resolution constraint of $\Delta z^+ \leq 0.4$ in the following simulations, to accurately model flows in RANS regions.

As a result, these examinations confirms the embedded WMLES functionality of SST-IDDES with STG for a flat plate flow. Thus, this method is basically verified for comparable geometry sections at the XRF1-UHBR configuration.

4 Grey-area investigation on nacelle-aircraft configuration

4.1 Geometry, flow conditions and RANS mesh

The actual target configuration consists of a half model of a modern transport aircraft configuration in conjunction with a through flow nacelle (cf. Fig. 3). The employed XRF1 aircraft model represents a wide-body long-range research configuration and is designed by Airbus. An Ultra High Bypass Ratio (UHBR) nacelle is integrated with the aid of a pylon and positioned close to the wing lower side. The UHBR design consists of an outer casing and a core body with plug. The casing is shaped circularly with a cross section similar to an airfoil. Both, nacelle and a specifically designed pylon were developed by DLR [1].

To find a suitable flow condition with shock-induced separation in the surrounding of the nacelle surface, a comprehensive numerical study was performed where various high speed off-design conditions were assessed. As key parameter for the occurrence of transonic shocks at a Reynolds number of $Re = 3.3$ million, a low angle of attack (α) was identified. For a farfield Mach number of 0.84 and $\alpha = -4°$, shock-induced separation is present at the wing lower side, the pylon and the nacelle. A single, locally separated transonic shock could be found at the outer surface of the nacelle lower side (cf. Fig. 4). Thus, a flow condition which allows to examine an isolated shock with subsequent boundary layer separation in the context of a nacelle-aircraft configuration was found.

In a preliminary work, a high-quality RANS mesh for the XRF1-UHBR half model was designed and constructed by projects partners of the research unit at the University of Stuttgart and DLR. The surface RANS mesh mainly consists of structured areas which are extruded to hexahedral blocks. These are designed to contain the entire RANS boundary layer with a safety factor of 2. The wall adjacent cell spacing fulfils $\Delta z^+ \leq 0.4$ and a growth rate of 1.12 is applied in wall-normal direction. A h-type
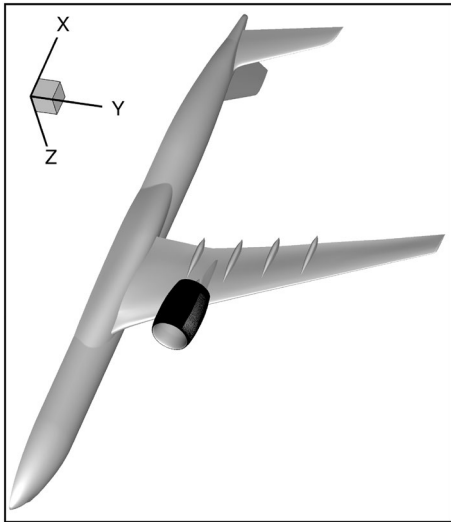
Fig. 3 Bottom view of XRF1-aircraft configuration with UHBR nacelle. The nacelle lower side includes the mesh refinement region for embedded WMLES

mesh topology is employed at the intersections of the aircraft components to be able to accurately resolve flow features in these areas. The farfield region is discretised by tetrahedra and extends to 50 wingspans in all coordinate directions. The total grid size before refinement amounts to 112 million points.
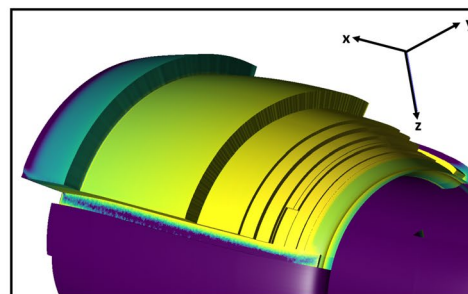
4.2 Grid design for embedded WMLES

In the following, the mesh design for the WMLES refinement region is introduced. A sophisticated meshing strategy, that aims to reduce the grid size as far as possible but follows basic refinement and extension constraints for WMLES, is developed. This is necessary in order to limit mesh size and resulting computing time to a reasonable level. Special care was taken to the mesh resolution of all coordinate directions which depend on the local boundary layer thickness δ. Additionally, a potential shock movement is considered with regard to the refinement extension as well as mesh resolution.

The refinement region is embedded within the previously described RANS mesh with the aid of unstructured bands in the surface mesh (cf. Figs. 4 and 5). This strategy allows to drastically increase the resolution within the structured boundary layer such that the surrounding RANS region remains unchanged. An unstructured nearfield block, which is also present in the pure RANS mesh, serves as an interface between the structured and the farfield block and exhibits a mesh decay rate of 0.85. The mesh decay rate quantifies the transition in grid resolution between high cell density (structured blocks) and low cell density (farfield block). The total mesh size of the combination of the RANS mesh and the refinement region for WMLES comprises 420 million points, with 280 million points used for the refined structured blocks (cf. Fig. 4 (right)).
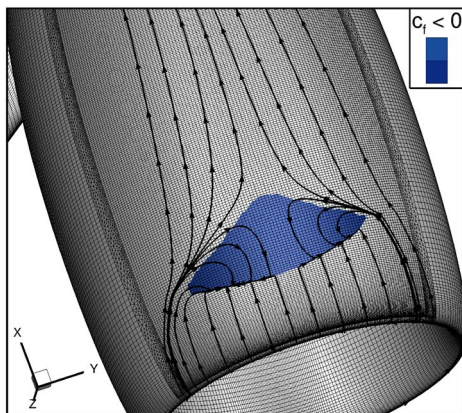
Fig. 4 Bottom view of the UHBR nacelle. Left: Area of recirculation of SST-RANS solution for $\mathbf{Ma_\infty = 0.84}$ and $\boldsymbol{\alpha = -4°}$. The shown RANS surface mesh already includes the boundaries for the refinement region in the form of unstructured streaks. Right: Extension of refinement area with stepwise increase in the streamwise direction. The colorbar visualises the cell surface area where yellow and purple represent large and low areas, respectively

Fig. 5 Surface mesh of refinement region on lower side of UHBR nacelle. Left: Discrete coarsening of $\Delta\varphi$ is apparent which subdivides the refinement area into five subregions. Right: Vertical unstructured (triangular based) streak enables to refine locally and keep surrounding RANS resolution untouched. Horizontal unstructured stripe allows to coarsen the spanwise resolution in streamwise direction
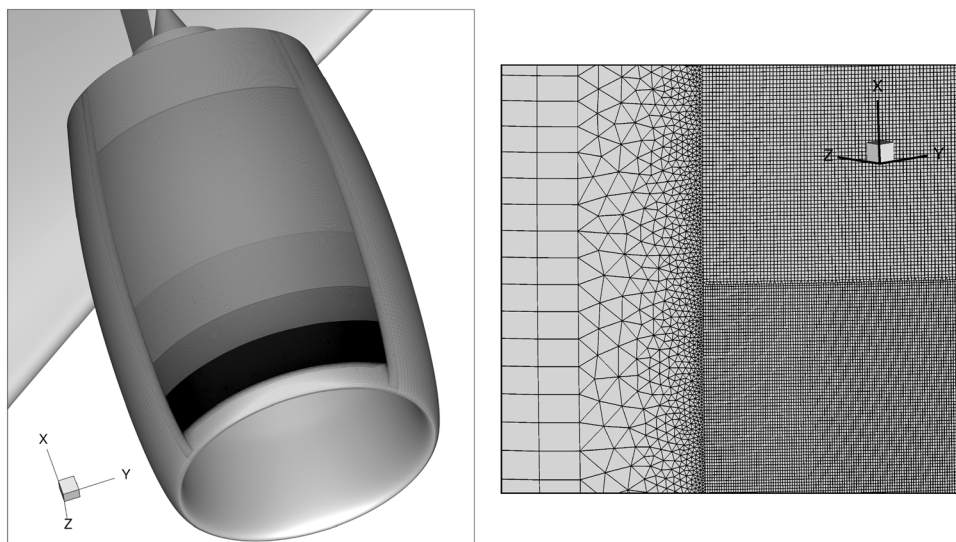
4.2.1 Extension of the refinement region

To describe locations on the nacelle surface more precisely, a cylindrical coordinate system r, φ and x/c is introduced, where c represents the nacelle chord length. Its reference point $r = 0$, $x/c = 0$ is located in the nacelle centre within a cross section that includes the entire nacelle leading edge. φ is set to 0° at the intersection between nacelle and pylon and increases in clockwise direction that 90° points towards the fuselage. In terms of grid resolution, a distinction is usually made between resolution in streamwise, spanwise and wall-normal direction. For the 3D flow about a nacelle, however, the term *spanwise direction* has to be further specified. Here, we define the term *spanwise* or *lateral direction* as equal to the local φ-base vector $\vec{e}_\varphi$ of the cylindrical coordinate system. Consequently, a cell length in *lateral* direction is equal to $r\Delta\varphi$.

According to [21], the first step in designing hybrid RANS LES mesh for DES-based algorithms is the definition of the RANS and LES regions for the given configuration. Since the aim of this research topic is the application of a WMLES methodology to a flow region with shock-induced separation, all flow regions directly related to this phenomenon are of interest and should be highly resolved. The primary region is the area of recirculation (AOR) downstream of the shock position (cf. Fig. 4 left). Flow regions related to this are the attached boundary layer upstream of the AOR and separated boundary layer downstream of the AOR until the trailing edge of the nacelle. To this end the average shock front position and extension of the AOR are calculated by a preceding SST-RANS calculation.

Figure 4 (left) shows a surface plot of a skin friction coefficient variable. It is defined as the product of the magnitude of the skin friction coefficient vector $|\vec{c}_f|$ and the sign of its x-component ($\mathrm{sgn}(c_{fx})$) and is referred to as c_f in the following.

In Fig. 4 (left), c_f is only plotted for $c_f < 0$, which serves as an indicator of the AOR. Since the boundary layers thickness is not only a function of x but also of φ we introduce the new variables $\delta_{\varphi,\max}(x)$ and $\delta_{\varphi,\min}(x)$ which refer to the maximum and minimum boundary layer thickness for a given streamwise position x.

The extension of the refinement region in spanwise direction ($\vec{e}_\varphi$) is chosen such that the entire area of recirculation is included with some margins at the lateral borders and extends 105° starting from 120° until 225° (cf. Fig. 4).

In x/c direction the refinement is applied between $x_a/c = 0.06$ and $x_b/c = 1$. The choice of $x_a/c = 0.06$ as the most upstream position is the result of the dependence of mesh resolution on the boundary layer thickness $\delta_{\varphi,\min}(x)$. The smaller the boundary layer thickness $\delta_{\varphi,\min}(x)$ at location x_a the smaller the required cell lengths $\Delta\zeta(x_a)$ in all coordinate directions $\zeta \in \{r, \varphi, x\}$ since $\Delta\zeta(x) \leq \delta_{\varphi,\min}(x)/10$. This in turn leads to a drastic increase of the total mesh size for decreasing x_a/c. The reason to place the end of the refinement region at the trailing edge of the nacelle ($x_b/c = 1$) was to avoid a WMLES–RANS transition near the nacelle surface. Such a transition across a viscous wall would require additional modelling techniques to ensure a seamless transition between WMLES and RANS areas and would increase model complexity. The refinement in wall-normal direction r is applied for wall distances that hold $d_w(x) \leq 1.2 \cdot \delta_{\varphi,\max}(x)$ in the interval $0.06 \leq x/c \leq 0.16$ and $d_w \leq 1.5 \cdot \delta_{\varphi,\max}(x)$ within $0.16 \leq x/c \leq 1$. Thus d_w/c ranges from 0.2% at $x/c = 0.06$ to 15% at the trailing edge (cf. Fig. 4 right). Although these distances are smaller than $d_w \leq 2 \cdot \delta(x)$ suggested by [22] we show in Sect. 5.3 that the

Fig. 6 Cross section of nacelle lower side at $\varphi = 180°$. Subregion Ω_1 ($0.06 \le x/c \le 0.16$) of the refinement region includes 200 Mio. cells which corresponds to 48% of the entire grid size
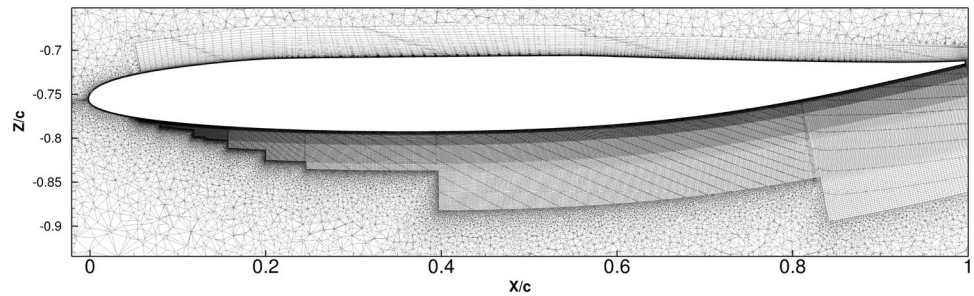
whole resolved boundary layer remains within the refined area with distance $d_{\mathrm{refined}}(x)$ over the entire simulated time period. Additionally, the extension of the refinement area in r-direction also considers a potential oscillation of the boundary layer separation point around its average position at $x_s/c = 0.13$ (SST-RANS solution). We assumed an oscillation amplitude of $\pm 0.03\,c$ which also allows to employ this mesh in case of a shock buffet. This amplitude was estimated from preliminary time-resolved experimental data (unsteady pressure-sensitive paint) of a XRF1 aircraft model with UHBR nacelle in the European Transonic Windtunnel (ETW). As a consequence, at position $x/c = 0.16$ a refinement distance of $d_{\mathrm{refined}}(0.16c) = 1.2 \cdot \delta_{\varphi,\max}(0.19c)$ is used.

4.2.2 Resolution of the refinement region

The resolution in x-direction depends on the local boundary layer thickness and is set to a limit of $\Delta x(x) \le \delta_{\varphi,\min}(x)/10$ which leads to a total number of 1350 points in x-direction from the leading edge to the trailing edge. Again an oscillation of separation due to shock buffet point is considered. Thus it is assumed to have an attached boundary layer until $x_s/c = 0.13 + 0.03$ leading to reduced boundary layer thickness compared to the preliminary SST-RANS solution. For this reason, the boundary layer thickness at $x/c = 0.16$ is estimated to $\delta_{\varphi,\min}(x/c = 0.08) \cdot 2^{4/5}$ according to turbulent boundary layer theory. As before, the lateral resolution is limited to $r\Delta\varphi(x) \le \delta_{\varphi,\min}(x)/10$. In contrast to the resolution in x-direction the adaption of $\Delta\varphi(x)$ to $\delta_{\varphi,\min}(x)$ is realised in a discrete manner. In this regard, the refinement region is separated into five subregions with its boundaries located at $x/c \in \{0.06;0.16;0.25;0.4;0.82;1\}$ (cf. Fig. 5). $\Delta\varphi(x)$ remains constant within each subregion Ω_i and is set to $r\Delta\varphi(x \in \Omega_i) = \delta_{\varphi,\min}(x_i)/10$ with x_i defined as the most upstream position of Ω_i. With this protocol the lateral resolution is always smaller than $\delta_{\varphi,\min}(x)/10$ which results in total numbers of $\{4350;1660;870;603;250\}$ points in $\vec{e}_\varphi$-direction within the corresponding subregion. Without this stepwise increase of $\Delta\varphi$, the total grid number would increase by a factor of 3 to $1.2 \cdot 10^9$ points. Again, a potential movement of the boundary layer separation point is considered and thus $r\Delta\varphi(x = 0.16c) = \frac{1}{10}\delta_{\varphi,\min}(x = 0.08c) \cdot 2^{4/5}$.

In r-direction the wall-normal spacing of the wall adjacent cells is limited to $\Delta r^+ = 0.4$. The cells of the entire refinement area are extruded geometrically with a growth factor of 1.12 until $\Delta r = \Delta x(x = 0.06c)$ is reached and Δr is initially kept constant to obtain locally isotropic cells. Since the distance of the refinement region $d_{\mathrm{refined}}(x)$ increases in x-direction in a cascading manner (cf. Fig. 4 (right) and 6) the geometric growth is continued for refinement areas with larger wall distances. Exemplarily, Δr is further increased to $\Delta r = \Delta x(x = 0.16c)$ for wall distances in the interval $d_{\mathrm{refined}}(x = 0.16c) \le r \le d_{\mathrm{refined}}(x = 0.25c)$ and applied, where $0.16 \le x/c \le 1$. Subsequently Δr is again increased until $\Delta r = \Delta x(x = 0.25c)$ for wall distances in the interval $d_{\mathrm{refined}}(x = 0.25c) \le r \le d_{\mathrm{refined}}(x = 0.4c)$ and applied where $0.25 \le x/c \le 1$. This protocol is repeated until Δr amounts to $\Delta r = \Delta x(x = 0.82c)$ for $d_{\mathrm{refined}}(x = 0.82c) \le r \le d_{\mathrm{refined}}(x = 1c)$ and $0.82 \le x/c \le 1$. Finally, the total number of grid points in wall-normal direction comprises $\{113; 168; 183; 230; 258\}$ points within the corresponding subregion.

4.3 Results of transient WMLES establishment

As initial solution for the SST-IDDES a converged SST-RANS solution was employed. The physical time step size amounts to $\Delta t = 5.5 \cdot 10^{-8}\,\mathrm{s} = 1/16750\,\mathrm{CTU}$ where $1\,\mathrm{CTU} = u_\infty \cdot c$ represents a single convective time unit (CTU). Δt is chosen that CFL < 1 is fulfilled for all grid cells. The RANS–LES interface and the Synthetic Turbulence Generator (STG) required for it are located at the streamwise position $x_{STG}/c = 0.06$.

Fig. 7 represents the temporal evolution of the Mach number in a cross section at $\varphi = 180°$ and four different times. With regard to the turbulent boundary layer thickness δ it should be noted that δ is entirely located within the refinement volume with sufficient distance to its boundary (indicated by black lines). After the depicted maximal extension at 0.5CTU the boundary layer thickness significantly decreases at later times. This decrease appears to be related with the shock movement in downstream direction since this correlation is also observed for various transonic
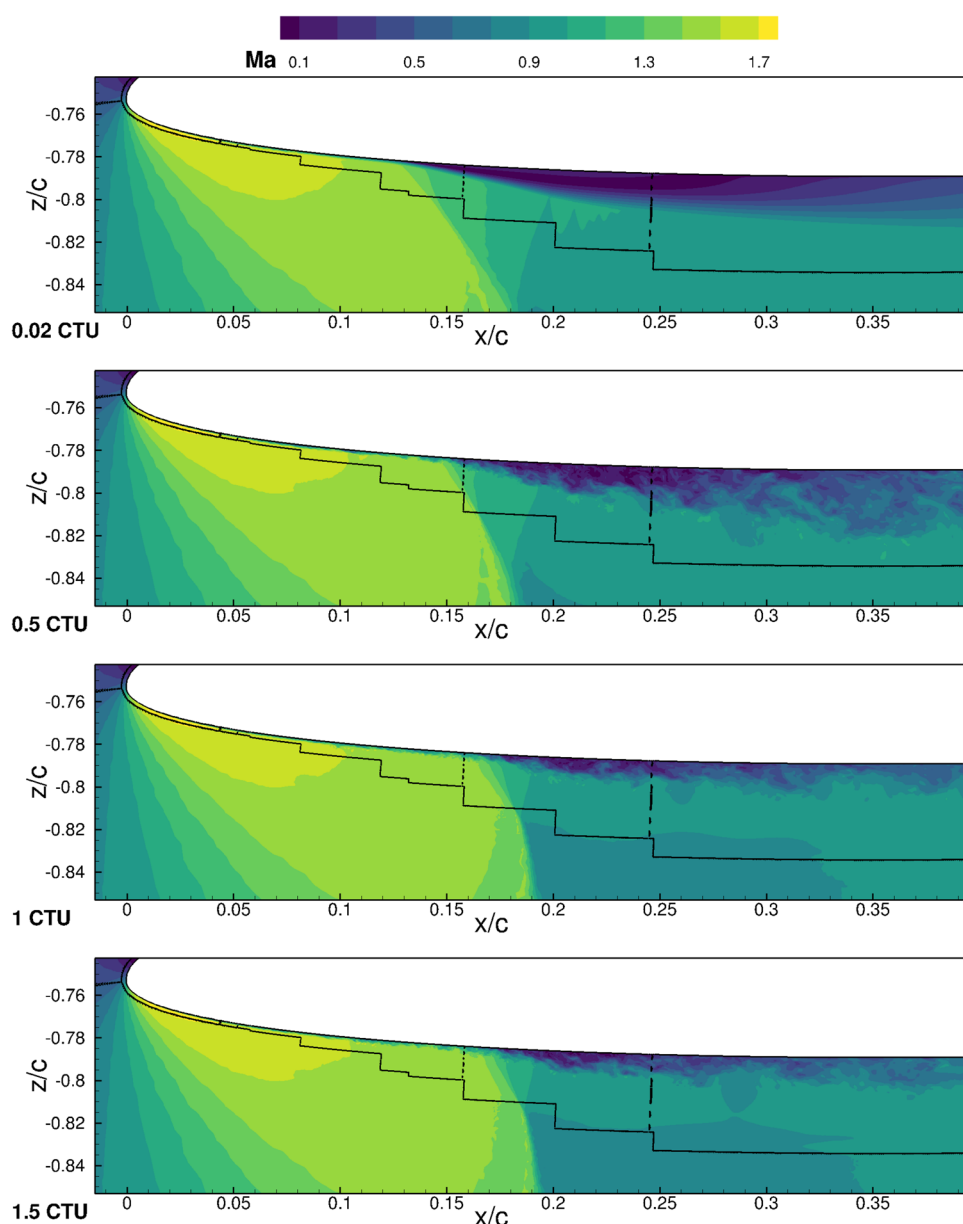
flows of wing profiles [23]. As mentioned before, the root of the shock front x_s is moving from its initial SST-RANS position $x_s(t_0) = 0.13c$ downstream to $x_s(t_{1\,CTU}) = 0.17c$ and remains at the same position until $x_s(t_{1.5\,CTU})$. Although x_s is located further downstream as we assumed for the mesh design ($0.1 \le x_s/c \le 0.16$), one has to note that such shock displacements are common in transient simulations (e.g. $t \le 7.5\,CTU$).

Another perspective on the temporal evolution is given in Fig. 8. Here, the c_f-distribution is shown at four different times. This figure confirms that the resolved turbulence develops over the entire refinement area. The transonic shock front is visible in form of a sudden decrease in c_f.

As in Fig. 7 it can be seen that the whole front is moving downstream until it remains in an area of $0.16 \le x_s/c \le 0.2$.

A critical effect appears at the lateral edges of the refined mesh where wedge-shaped regions with low values of c_f are present. This problem has several reasons and is difficult to circumvent as explained in the following. One reason is due to the modelling setup, since the STG forcing domain was chosen to be a bit narrower than the EWMLES region in order to avoid possibly adverse interactions of synthetic turbulence with RANS modelling, leaving two small gaps at the lateral edges. Consequently, regions with little resolved and significantly reduced modelled turbulence exist. This issue, however, could be attenuated by ensuring a direct lateral connection of the STG forcing domain to the RANS
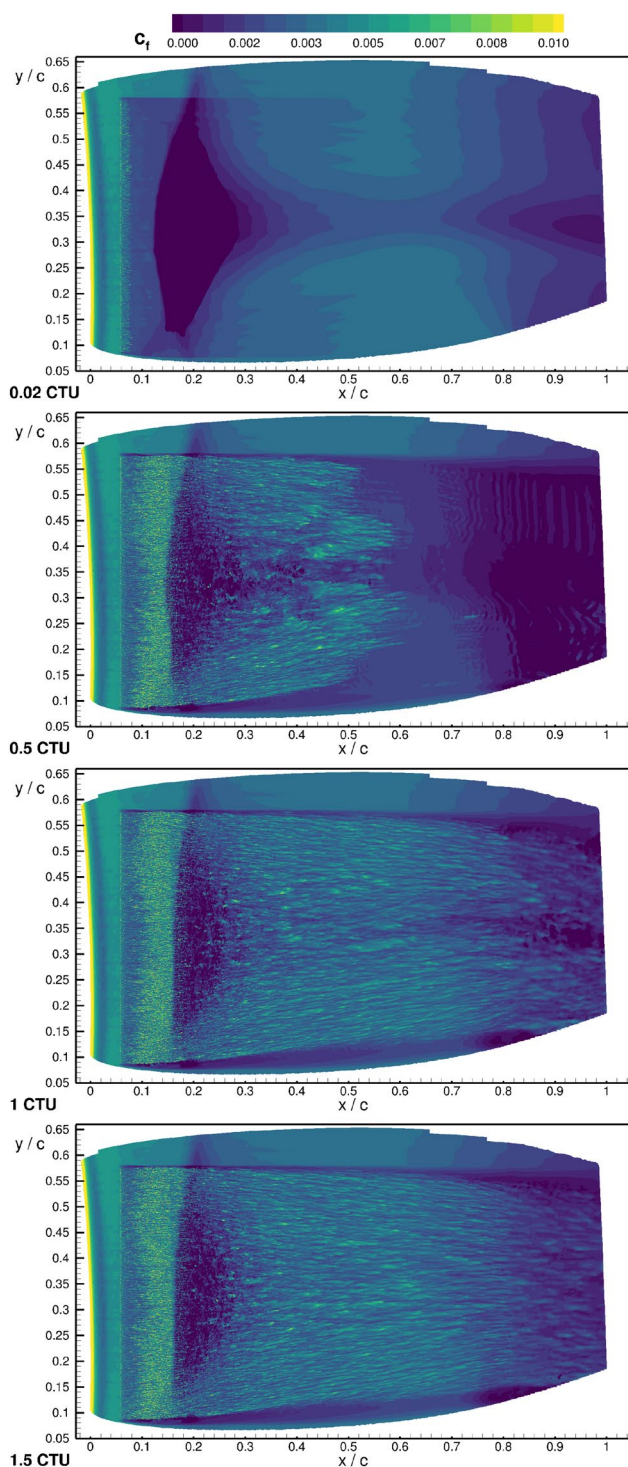
Fig. 8 Temporal evolution of c_f-distribution within the refinement area on projected nacelle surface

regions. Nevertheless, even with a direct connection at this streamwise location, vortices directly located in the lateral RANS–LES interface would be treated partly with URANS and partly with WMLES. Furthermore, it is unlikely that the alignment of the lateral RANS–LES interface is exactly

parallel to the flow direction further downstream, especially for a 3D configuration subject to large-scale flow unsteadiness (e.g. shock movement). Thus, the flow may enter from the RANS into the EWMLES zone, since no STG is employed at the lateral borders. Consequently, a severe grey-area effect may arise in case of an even more pronounced lateral flow. Nevertheless, as visible in Fig. 8 the described phenomenon is limited to the lateral boundaries and does not affect the actual focus region. However, we want to emphasise that such lateral grey areas are an unsolved issue in hybrid RANS–LES of complex 3D flow, in particular in strictly zonal setups. In future investigations, we plan to consider a setup in which the self-adaptive (i.e. non-zonal) IDDES is allowed to switch by itself between RANS and WMLES at the lateral borders, even though this will probably not solve all the mentioned issues.

To give an impression of the vortex structure of the resolved turbulence an isosurface of the Q-criterion ($Q = 10^{10}$) at $t = 1.5$ CTU is depicted in Fig. 9. As already observed in Fig. 8 an extensive formation of turbulent structures within the refinement region is present. These structures are growing with increasing streamwise position and partially evolve into hairpin vortices which corresponds to expected flow behaviour.

4.4 Investigation of grey area

This section focuses on the transitional region from modelled to fully resolved turbulence downstream of the RANS–LES intersection, which is located at streamwise position $x/c = 0.06$. A way to describe the transition from modelled to resolved turbulence is to consider the (modelled) eddy viscosity μ_t in relation to the laminar viscosity μ_l. Figure 10 shows the distribution of μ_t/μ_l in a xz-plane at $\varphi = 180°$ for $t = 1.5$CTU. A rapid reduction of the modelled turbulence by a factor of 10 is observed downstream of the RANS–LES interface, which is solely achieved by setting $f_{dt} = 1$ in the target WMLES region, see Sect. 3.1. This is why we refrain from applying additional damping methods at the RANS–LES interface. In addition, the significant decrease of the modelled turbulence allows to draw conclusions about the mesh resolution, since μ_t is proportional to the squared cell spacing in the LES regions. Thus, in accordance with the careful consideration of common mesh resolution criteria as described in Sect. 5.2.2, the very low level of μ_t/μ_l in these regions gives another indication that the grid resolution in the boundary layer is adequate.

In the following, a quantitative analysis of the grey area / adaption region is performed. To this end, the flow field was averaged with regard to time and spanwise direction. The temporal average was applied for $0.42 \leq t/\text{CTU} \leq 1.5$. The start time $t = 0.42$ is chosen such that the resolved turbulence is completely established within the focus region

Fig. 9 Isosurface of Q-Criterion ($Q = 10^{10}$) at nacelle lower surface for LD2 scheme at $t = 1.5\,\text{CTU}$
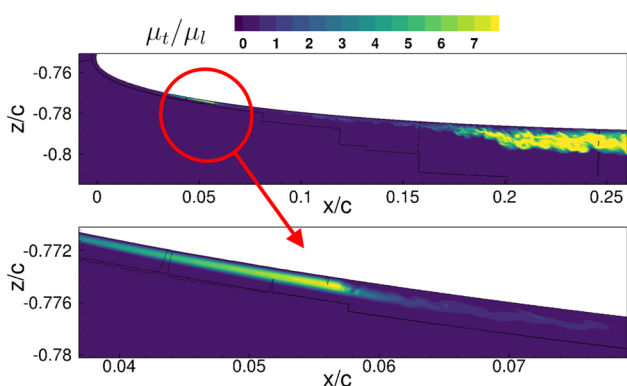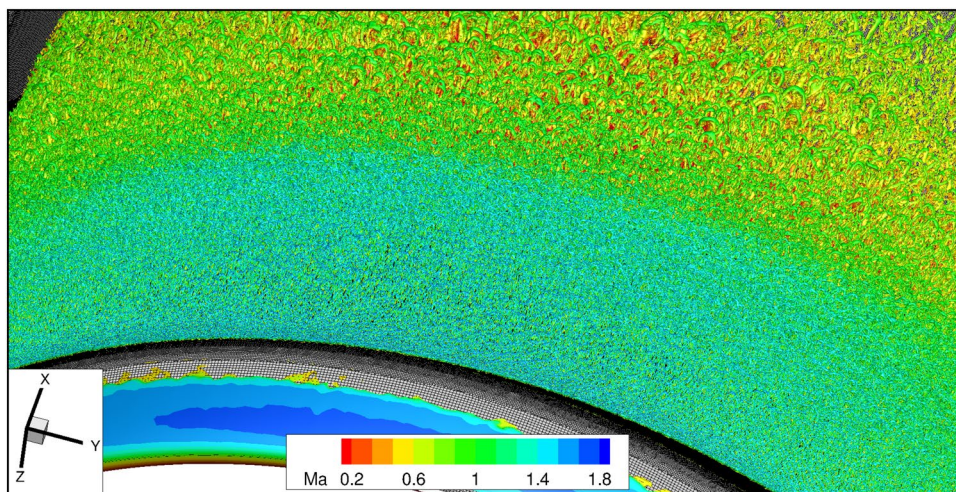

Fig. 10 Level of modelled turbulence expressed through μ_t/μ_l in a xz-plane at $\varphi = 180°$ below the nacelle outer surface

($0.06 \le x/c \le 0.25$) and no remains of the initial RANS solution are present in this area (cf. Fig. 8 at $t = 0.5\,\text{CTU}$). Since the flow about the nacelle is partly rotationally symmetric a spatial average along this coordinate direction (lateral direction $\vec{e}_\varphi$) was computed. This rotational symmetry is visible in the projected surface distributions of Fig. 8 (for $t \ge 0.5\text{CTU}$) within the streamwise interval $0.06 \le x/c \le 0.16$ of the refinement region. The spanwise average was applied such that the areas of underresolved turbulence at its borders were omitted ($\varphi \in [125°; 220°]$).

Figure 11 (top) shows the result of the EWMLES mean pressure distribution (mean-c_p) along with the initial RANS solution. Good agreement between these curves are present for $x/c \le 0.13$ where $x/c = 0.13$ is the average location of the shock front of the SST-RANS solution which results into a sudden rise in mean-c_p. It is apparent that this agreement also persists for positions upstream of the STG ($x/c \le 0.06$) which indicates that no upstream effect of the STG exists. With regard to the EWMLES shock position the already

described shift in downstream direction is also present in this depiction and located at $x/c = 0.15$. Due to the comparatively early start in the averaging of mean-c_p it is not reasonable to compare the curves for $x/c \ge 0.3$ since transient effects from the switch from RANS to EWMLES still exist in this area.

A further quantitative flow comparison between SST-RANS and EWMLES is given in Fig. 11 (bottom) which shows mean skin friction distributions (mean-c_f). In this paragraph, we especially focus on the spatially averaged mean-c_f distribution (red curve). In the flow region upstream of the STG ($x/c \le 0.06$) good agreement are visible again which confirms the previously mentioned absence of potential STG upstream effects. However, for $0.06 \le x/c \le 0.16$ remarkable deviations appear. One observes a significant drop in mean-c_f (red curve) directly downstream of the STG at $x/c = 0.07$ of 33 % and a subsequent increase with a peak value at $x/c = 0.13$. The skin friction adaption length which measures the distance between STG position and the subsequent peak in mean-c_f amounts to $46\,\delta_{STG}$ where δ_{STG} represents the boundary layer thickness at the STG position. A further analysis and discussion of the mean-c_f deviations is given in Sect. 5.6. Considering now the region where $0.16 \le x/c \le 0.25$ we observe that the region of recirculation has disappeared, at least for this transient period of time averaging since the laterally averaged mean-c_f is always positive. However, this does not imply, that the local (not laterally averaged) skin friction is always positive, too. As visible in Fig. 11, the local mean-c_f distribution at $\varphi = 180°$ still exhibits an area of recirculation. At the streamwise positions $x/c = 0.25$ and $x/c = 0.40$, which corresponds to locations of the $\Delta\varphi$ coarsening steps of the mesh (cf. Sect. 5.2.2), additional distortions in the EWMLES mean-c_f distribution appear. This indicates that the local mesh resolutions of
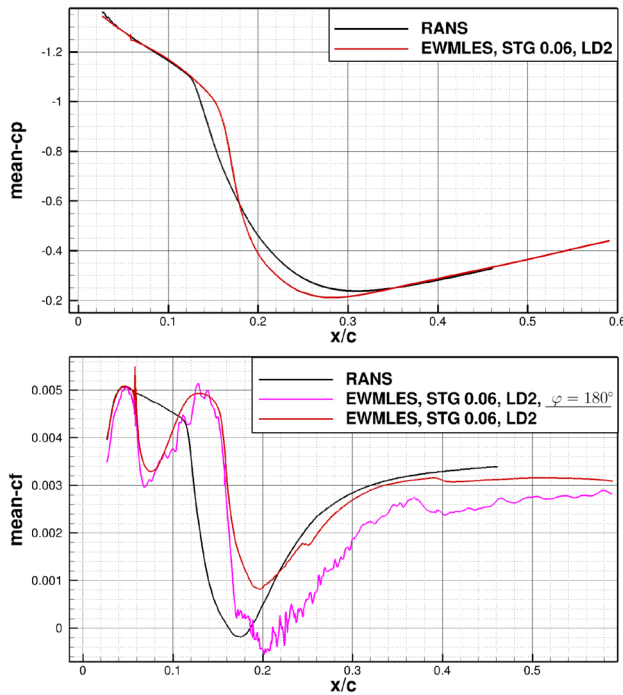
Fig. 11 Quantitative comparison of time and spanwise averaged pressure (top) and skin friction distributions (bottom) in streamwise direction between the initial RANS and EWMLES solutions. In addition, a not laterally averaged mean-c_f distribution passing through the centre of the WMLES region ($\varphi = 180°$) is shown (pink line)

$r\Delta\varphi = \delta_{\varphi,min}/10$ might be locally at the lower limit at these positions.

To provide further insights into the turbulent boundary layer in the vicinity of the RANS–LES interface, wall-normal profiles of turbulent kinetic energy (TKE) and mean velocity (mean-u) in the lateral centre of the refinement region ($\varphi = 180°$) are analysed. Figure 12 contains TKE-profiles of the immediate RANS–LES vicinity (left) as well as the further development downstream (right). A main finding of Fig. 12 (left) is the fast generation of

resolved turbulent kinetic energy in the EWMLES between $x/c = 0.05$ (black dashed curve) and $x/c = 0.07$ (green dashed curve), despite some delay compared to the RANS reference. The highest difference in the total TKE (sum of modelled and resolved TKE) occurs at a wall distance of $d_w/\delta_{STG} = 0.25$ and amounts to 0.18 % (cf. solid green and black line of Fig. 12 left). This drop of total TKE compared to RANS is however significantly smaller than for mean-c_f at $\varphi = 180°$, which amounts to a maximum of 40% (see Fig. 11). Comparing the TKE of the EWMLES and RANS solutions at $x/c = 0.07$ (solid green line and green squares) there are significant differences in the outer boundary layer, while the TKE of the inner boundary layer match for both simulations.

The further development of the boundary layer shows a strong increase of the total TKE in the EWMLES (cf. solid green line in Fig. 12 (left) with orange and red solid lines in Fig. 12 (right)). The values at $x/c = 0.09$ and $x/c = 0.11$ are even higher than the RANS reference values (orange and red squares in Fig. 12 (right)). It is noticeable that the maximum values of the RANS TKE-profiles do not increase in streamwise direction, but, in good agreement with the total WMLES TKE-profiles, widen in the wall-normal direction.

As an interim result, the strong drop in the mean-c_f distribution is not reflected by an equally strong under-prediction of TKE, suggesting that the outer boundary layer development is only mildly affected by the grey-area issue. This is confirmed by an additional analysis of mean velocity profiles in the same region, cf. Figure 13. For all velocity profiles shown, there is good agreement between the RANS and EWMLES solutions in the outer boundary layer ($d_w/\delta_{STG} > 0.4$), suggesting that the RANS–LES transition mainly affects the near-wall velocity (gradient), i.e. mean-c_f (see Fig. 11), and to a lesser extent the overall boundary layer development.

Fig. 12 Turbulent kinetic energy (TKE) profiles at different streamwise positions at $\varphi = 180°$ from EWMLES and a reference RANS simulation. The wall distance d_w and TKE are normalised with the local boundary layer thickness δ at the position of the STG ($x_{STG}/c = 0.06$) and the squared farfield velocity u_{inf}, respectively. Left: Profiles in the vicinity of the RANS–LES interface. Right: Profiles at further downstream positions
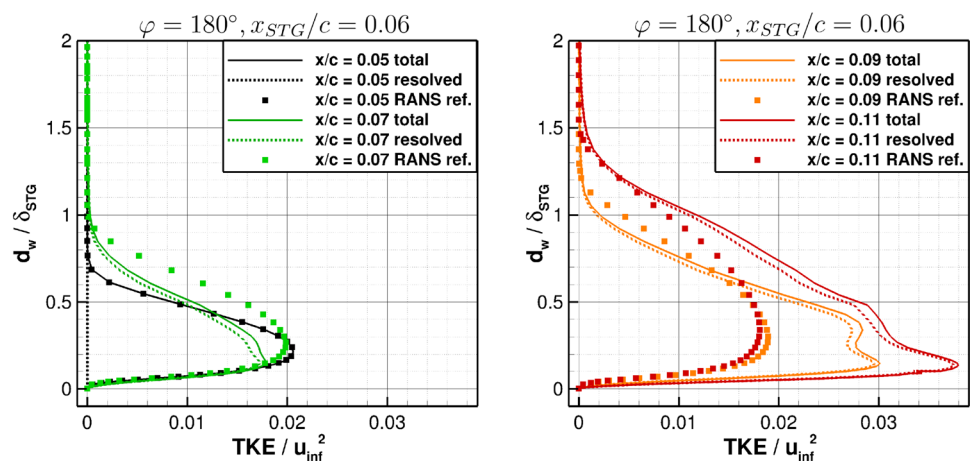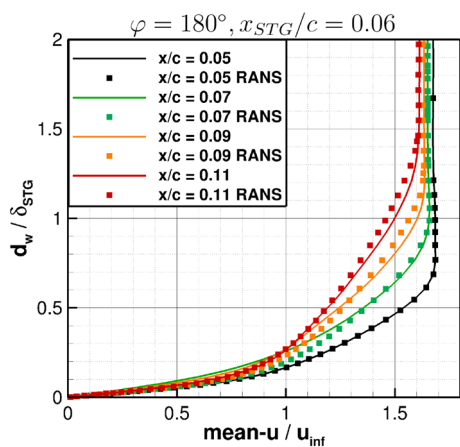
Fig. 13 Time-averaged velocity profiles of the EWMLES solution (lines) and the reference RANS result (squares) at $\varphi = 180°$ near the RANS–LES interface ($x_{STG}/c = 0.06$)

4.5 Sensitivity studies

4.5.1 Positioning of the RANS–LES interface

Preliminary grid number estimations for different locations of the RANS–LES interface in x-direction (x_{STG}) demonstrated a strong dependence of x_{STG} and the total grid number. A shift of this boundary in downstream direction allows to reduce the total grid number significantly. Exemplarily, moving x_{STG} by $0.02c$ enables to reduce the total grid size about 100Mio points without violating the applied extension and resolution constraints for the refinement area. This dependence is a consequence of the shortening of the refinement area in x-direction by which the subregion with the highest cell density is narrowed. Also, due to the dependence of $\Delta\varphi_{\Omega_1}$ on $\delta_{\varphi,min}(x_{STG})$ in subregion Ω_1 it is possible to increase $\Delta\varphi_{\Omega_1}$ in the entire interval $x/c \in [x_{STG};0.16]$ (cf. 5.2.2).

This dependency on the STG position suggests to place the RANS–LES boundary as close as possible to the shock front and examine its effect on the flow solution. Based on the original assumption that the c_f-adaption length of the STG amounts less than $10\,\delta_{STG}$ we estimated $x_{STG}/c = 0.08$ as latest possible position in order to avoid direct interactions with the shock front. Additionally, for this estimation a potential shock movement in upstream direction until $x_{s,min} = 0.1$ was taken into account. For the following examinations we used the same mesh as before to verify a basic applicability of a late RANS–LES interface.

Figure 14 shows mean-c_p and mean-c_f distributions of the EWMLES results for $x_{STG}/c = 0.08$ (green curves) where the same averaging procedure as in Sect. 5.4 is employed. It is striking that the mean-c_p distribution is
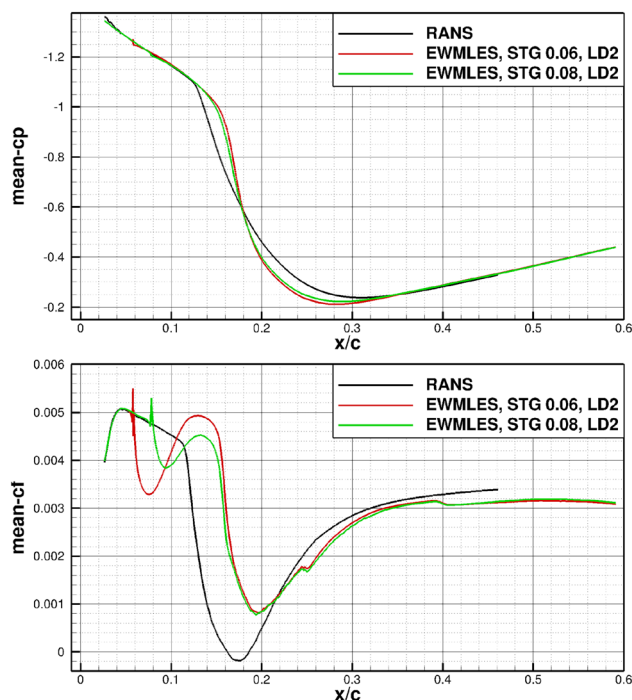
Fig. 14 Effect of positioning of the RANS–LES interface on averaged surface pressure and skin friction distributions

almost identical to the previous $x_{STG}/c = 0.06$ result (red) with maximum deviations of two line thicknesses for $x/c \geq 0.16$. However, with respect to mean-c_f and its adaption area downstream of the STG distinct differences compared to the $x_{STG}/c = 0.06$ result exist. First, the initial decay is significantly weaker than before. Furthermore, its adaption length is reduced and only amounts to $19\,\delta_{STG}$ so that its peak is located at almost the same position as for the $x_{STG}/c = 0.06$ result. The peak value though, is significantly reduced and corresponding to the initial RANS solution directly upstream of the shock position. A further discussion of these features of the adaption regions is given in Sect. 5.6. It is remarkable that for $x/c \geq 0.16$ the subsequent mean-c_f evolution is almost identical to the $x_{STG}/c = 0.06$ result which demonstrates an independence of the flow solution with regard to the location of the RANS–LES interface. However, a potential reason for the shorter skin friction adaption length and the mentioned similarities of mean-c_f distributions might be due to the strong disturbance introduced by the transonic shock. This shock could superimpose upstream effects in the boundary layer. Thus, for an equivalent subsonic case the adaption lengths could again be similar for both interface locations.

Fig. 15 Isosurface of Q-Criterion ($Q = 10^{10}$) for reference central scheme at nacelle lower at $t = 1.5$ CTU
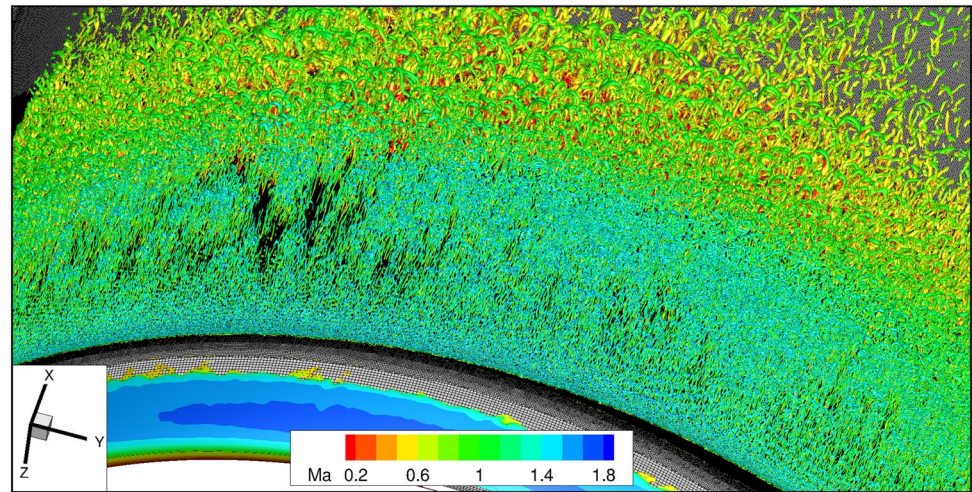
4.5.2 Impact of numerical scheme

A further objective of our research was to compare the effect of different numerical schemes for the central discretisation of viscous fluxes which is applied in the refinement region (LES). In addition to the already employed LD2 scheme (Sect. 3.3) a reference central scheme (Eq. 8 in Sect. 3.3) is applied on the same numerical setup as in Sect. 5.4. Although the necessity of the high-quality LD2 scheme against the reference scheme has been demonstrated with the aid of the DIT test case in 4.1 it is not obvious how the reference scheme performs for transonic flows on a 3D configuration. To give a qualitative impression of the flow field the Q-Criterion at $Q = 10^{10}$ for a snapshot at $t = 1.5$ CTU is shown in Fig. 15 which can directly compared to Fig. 9. The comparison shows that the previous formation of turbulent structures is now partially interrupted. Especially the region directly downstream of the STG lacks turbulent structures. It is striking that coarser structures such as the clearly visible horseshoe vortexes are preserved whereas tiny structures are vanished. This is in direct agreement with the results from the DIT test case which demonstrates that small turbulent scales are strongly damped by the reference scheme (cf. Fig. 1).

These observations are also present in the analysis of the average skin friction distribution (blue curve in Fig. 16). Whereas the mean surface pressure is hardly affected by the numerical scheme, mean-c_f shows large deviations. Especially the decay downstream of the STG indicates a lack of resolved turbulence. Additionally, compared to the LD2 results the mean-c_f level is underestimated in the area downstream of the shock-boundary layer interaction ($0.35 \leq x/c \leq 0.6$). This confirms the previous observation of Fig. 15 of underresolved turbulence throughout the entire refinement region.

4.6 Reynolds number and mesh resolution effect on STG-adaption region

In the following, we address the so far unsound behaviour of the skin friction adaption region downstream of the STG arising for the XRF1 configuration.

As already described before the c_f-adaption region displays the largest deviations with regard to streamwise extension as well as maximal and minimal mean-c_f-deviations for the nacelle at $x_{STG} = 0.06c$. These features reduce for $x_{STG} = 0.08c$ and vanish for the flat plate test case (cf. Fig. 2 and 14). A closer look into the flow properties and mesh resolution at the location of the STG suggests a dependency on $Re_{\delta,STG}$ (Table 1). Here, $Re_{\delta,STG}$ is defined as a Reynolds number referring to the local boundary layer thickness δ_{STG} as well as velocity and kinematic viscosity at the outer edge of δ_{STG}. This Reynolds number, which directly impacts the input statistics of the STG, has its lowest number for the nacelle case at $x_{STG} = 0.06c$ (4989) and increases for $x_{STG} = 0.08c$ (6975) and the flat plate flow (24200). The ratio of turbulent and laminar viscosity (max (μ_t/μ_l)) which serves as measure of modelled turbulence shows a comparable trend. Since low Reynolds numbers enhance the stability of the boundary layer and hence suppress turbulent fluctuations, this might lead to a damping of the injected turbulent structures. As a consequence the boundary layer evolves into a flow with significantly reduced turbulence which is visible in a strongly reduced level of mean-c_f. Thus, it appears that the distinct c_f-adaption region can be traced back to a low-Reynolds number effect.

A further reason might be due to the lateral mesh resolution Δy or $r\Delta\varphi$, which amounts to $\Delta y = \delta/20$ for the flat plate flow and coarsens to $\delta/16$ at $x_{STG} = 0.08c$ and $\delta/12$ at $x_{STG} = 0.06c$ for the nacelle flow (cf. Table 1). Since a lateral resolution of $\Delta y = \delta/20$ is actually defined as coarsest
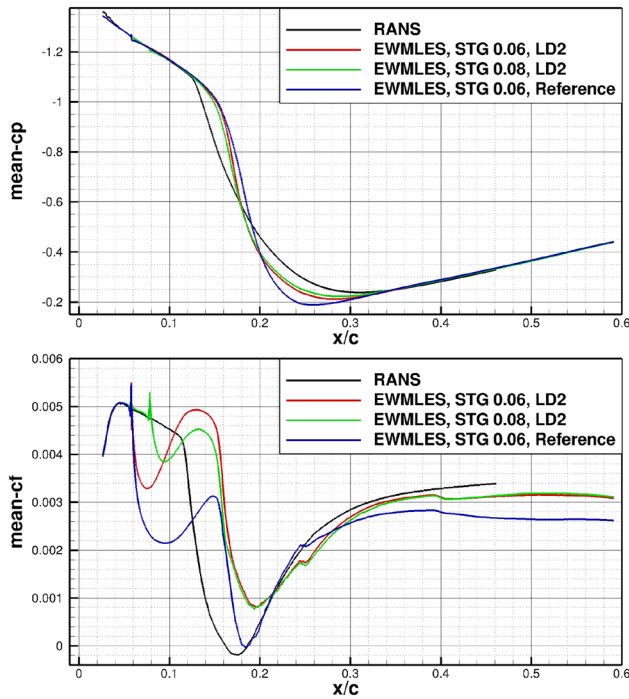
Fig. 16 Effect of different numerical schemes on averaged surface pressure and skin friction distributions

resolution the present somewhat coarser resolutions might perturb a proper development of the turbulent boundary layer [3]. Another difference between the nacelle and the flat plate is the respective streamwise pressure gradient which might have an influence on the adaption region.

Therefore, further examinations on flat plate flows for lower Re_∞ (resulting in smaller Re_δ) as well as coarser resolutions Δy will be performed in future work to provide a verification of the here detected correlations.

5 Conclusions

A scale-resolving WMLES methodology in conjunction with the SST turbulence model was applied to the XRF1 aircraft configuration with UHBR nacelle at transonic flow conditions. The method was applied locally at the nacelle surface to examine shock-induced separation. A Synthetic Turbulence Generator (STG) was employed to enhance the transition from modelled to resolved turbulence at the RANS–LES interface.

Prior to the actual examination on the aircraft configurations basic functionalities of the methodology were successfully verified for flows of decaying isotropic turbulence and flows over a flat plate for $Re_\theta = 3030$.

With regard to the target configuration, a sophisticated mesh which refines 32 % of the nacelle outer surfaces and comprises 420 million grid points was constructed. The main features of the mesh design are the dependence of mesh resolution (Δx, Δy and Δz) on the local boundary layer thickness and the consideration of a potential shock movement due to buffet.

Analysis of the transient process of the simulation showed a well resolved formation of turbulent structures over almost the entire refinement region with a broad spectrum of turbulent scales. It has been demonstrated that these features are also the result of the employed LD2 scheme. For a reference central scheme with higher artificial dissipation, small turbulent scales are damped leading to globally underresolved turbulence.

Another outcome of this study is the observation that the STG-adaption region (with regard to the skin friction) correlates to the local Reynolds number as well as mesh resolution in spanwise direction (cf. Sect. 4.6). For decreasing Reynolds numbers and coarser mesh resolutions an increasing skin friction adaption length and more distinct decay in the c_f-distribution were observed. However, analysis of boundary layer profiles in the RANS–LES interface has shown that the interface only adversely affects the skin friction distribution, whereas the overall boundary layer is mildly affected.

We still assume that a strong disturbance in c_f should be avoided in order to rule out any interference of the grey area with the transonic shock front. Therefore, sufficient distance between the STG and the shock front is required, which might not be given for of a more upstream shock position (e.g. in case of strong shock buffet). For this reason, further research on the sensitivities of the adaption length in the flat-plate case is planned w.r.t. the lateral grid resolution, the local Reynolds number and the streamwise pressure gradient.

Table 1 Comparison of several local flow quantities at the location of the synthetic turbulence generator for all presented configurations

	Re_∞	δ_{STG}/m	$Re_{\delta,STG}$	Δx	Δy or $r\Delta\varphi$	max $\left(\mu_t/\mu_l\right)$
Flat Plate	4.7 Mio	0.006	24200	$\delta/10$	$\delta/20$	87
Nacelle	3.3 Mio	0.00024	4989	$\delta/11.2$	$\delta/11.76$	9
$x_{STG} = 0.06c$						
Nacelle	3.3 Mio	0.00033	6975	$\delta/13.75$	$\delta/16.17$	10
$x_{STG} = 0.08c$						

Δx refers to the local streamwise grid spacing and Δy or $r\Delta\varphi$ to the local spanwise grid spacing

Declarations

References

1. Spinner, S., Rudnik, R.: Design of a UHBR through flow nacelle for high speed stall wind tunnel investigations. Deutscher Luft- und Raumfahrt Kongress (2021)
2. Cécora, R.D., Radespiel, R., Eisfeld, B., Probst, A.: Differential reynolds-stress modeling for aeronautics. AIAA J. **53**(3), 739–755 (2015)
3. Shur, M.L., Spalart, P.R., Strelets, M.K., Travin, A.K.: A hybrid rans-les approach with delayed-des and wall-modelled les capabilities. Int. J. Heat Fluid Flow **29**(6), 1638–1649 (2008)
4. Travin, A., Shur, M., Strelets, M., Spalart, P.R.: Physical and numerical upgrades in the detached-eddy simulation of complex turbulent flows. Adv. LES Complex Flows **65**(5), 239–254 (2002)
5. Schwamborn, D., Gerhold, T., Heinrich, R.: In: Wesseling, P., Oñate, E., Périaux, J. (eds.) ECCOMAS CFD, ed. by M. Braza, A. Bottaro, M. Thompson. TU Delft (2006)
6. Menter, F.R.: Two-equation eddy-viscosity turbulence models for engineering applications. AIAA J. **32**(8), 1598–1605 (1994)
7. Gritskevich, M.S., Garbaruk, A.V., Schütze, J., Menter, F.R., et al.: Development of ddes and iddes formulations for the k-ω shear stress transport model. Flow Turbul. Combust. **88**(3), 431 (2012)
8. Probst, A., Schwamborn, D., Garbaruk, A., Guseva, E., Shur, M., Strelets, M., Travin, A.: Evaluation of grey area mitigation tools within zonal and non-zonal rans-les approaches in flows with pressure induced separation. Int. J. Heat Fluid Flow **68**, 237–247 (2017)
9. Adamian, D., Travin, A.: In: Kuzmin, A. (ed.) Computational fluid dynamics, pp. 739–744. Springer, Berlin (2011). https://doi.org/10.1007/978-3-642-17884-9
10. Francois, D.G., Radespiel, R., Probst, A.: Forced synthetic turbulence approach to stimulate resolved turbulence generation in embedded LES. Notes Numer. Fluid Mech. Multidiscip. Des. **130**, 81–92 (2015). https://doi.org/10.1007/978-3-319-15141-0_6
11. Probst, A., Ströer, P.: Comparative assessment of synthetic turbulence methods in an unstructured compressible flow solver. Notes Numer. Fluid Mech. Multidiscip. Des. **143**, 193–202 (2020). https://doi.org/10.1007/978-3-030-27607-2_15
12. Probst, A., Löwe, J., Reuß, S., Knopp, T., Kessler, R.: Scale-resolving simulations with a low-dissipation low-dispersion second-order scheme for unstructured flow solvers. AIAA J. **54**(10), 2972–2987 (2016)
13. Kok, J.: A high-order low-dispersion symmetry-preserving finite-volume method for compressible flow on curvilinear grids. J. Comput. Phys. **228**(18), 6811–6832 (2009)
14. Löwe, J., Probst, A., Knopp, T., Kessler, R.: Low-dissipation low-dispersion second-order scheme for unstructured finite-volume flow solvers. AIAA J. **54**(10), 2961–2971 (2016)
15. Probst, A., Melber-Wilkending, S.: Hybrid RANS/LES of a generic high-lift aircraft configuration near maximum lift. Int. J. Numer. Methods Heat Fluid Flow **32**(4), 1204–1221 (2022). https://doi.org/10.1108/hff-08-2021-0525
16. Comte-Bellot, G., Corrsin, S.: Simple Eulerian time correlation of full-and narrow-band velocity signals in grid-generated,'isotropic'turbulence. J. Fluid Mech. **48**(2), 273–337 (1971)
17. Kraichnan, R.H.: Diffusion by a random velocity field. Phys. Fluids **13**(1), 22–31 (1970)
18. Probst, A.: Implementation and assessment of the synthetic-eddy method in an unstructured compressible flow solver. Notes Numer. Fluid Mech. Multidiscip. Des. **137**, 91–101 (2018). https://doi.org/10.1007/978-3-319-70031-1_7
19. Laraufie, R., Deck, S.: Assessment of Reynolds stresses tensor reconstruction methods for synthetic turbulent inflow conditions. Application to hybrid RANS/LES methods. Int. J. Heat Fluid Flow **42**, 68–78 (2013). https://doi.org/10.1016/j.ijheatfluidflow.2013.04.007
20. Nagib, H.M., Chauhan, K.A., Monkewitz, P.A.: Approach to an asymptotic state for zero pressure gradient turbulent boundary layers. Philos. Trans. R. Soc. A **365**(1852), 755–770 (2007)
21. Spalart, P.R., Streett, C.: Young-person's guide to detached-eddy simulation grids. NASA Technical Reports Server (2001)
22. Menter, F.R.: Best practice: scale-resolving simulations in ansys cfd. ANSYS Ger. GmbH, pp 1–75 (2012)
23. Jacquin, L., Molton, P., Deck, S., Maury, B., Soulevant, D.: Experimental study of shock oscillation over a transonic supercritical profile. AIAA J. **47**(9), 1985–1994 (2009)